ELSEVIER

Contents lists available at ScienceDirect

International Journal of Fatigue

journal homepage: www.elsevier.com/locate/ijfatigue



Fatigue crack propagation in [0 1 2] NiTi single crystal alloy

E. Sgambitterra^{a,*}, C. Maletta^a, F. Furgiuele^a, H. Sehitoglu^b

- ^a University of Calabria, Department of Mechanical, Energy and Management Engineering, Italy
- ^b University of Illinois at Urbana-Champaign, Department of Mechanical Science and Engineering, USA



ARTICLE INFO

Keywords:
Shape memory alloys
Fatigue crack propagation
NiTi single crystal
Digital image correlation
Over-deterministic method

ABSTRACT

Fatigue crack propagation experiments on nickel titanium single crystal alloy, with [012] crystallographic orientation, were carried out in this study. Stable microstructure, i.e. stable austenite and stable martensite, with the same chemical composition, were investigated. To this aim, two different values of temperature were analyzed. The digital image correlation (DIC) technique was used to obtain the displacement experienced by the sample during the application of the load. Obtained data were used as input parameters of a numerical procedure, that is able to estimate the effective stress intensity factor the sample actually experiences. The procedure is also able to automatically calculate the effective crack length. Numerical crack opening displacement measurements were also conducted in order to estimate the near crack tip stiffness of the microstructures. Results revealed that the stable austenite exhibits a lower threshold value of the stress intensity factor and a higher crack growth rate. Furthermore, it was demonstrated that, when dealing with martensite, local elastic properties change, as a consequence of the variants reorientation, and this effect has to be taken into account for the fatigue crack growth characterization.

1. Introduction

Shape memory alloys (SMAs), and in particular the Nickel Titaniumbased ones (NiTi), received considerable interest from the scientific and engineering communities in recent years, thanks to their unique properties, namely shape memory effect (SME) and superelastic effect (SE) [1]. In particular, these peculiarities allow the material to recover large deformations as a result of the reversible solid-state phase transition between austenite and martensite. Such transformation can be activated by a change of the operating temperature (TIM, thermally-induced martensite) or by the application of an external mechanical stress (SIM, stress-induced martensite). Due to these interesting features, as well as their good mechanical performances and biocompatibility, NiTi alloys are highly used in many branches of engineering and medicine [2,3], even though in most fields their applicability is currently limited by lack of design methodologies and material knowledge, especially when dealing with fatigue damage, i.e. with crack nucleation and propagation.

Therefore, many studies were carried out to better investigate on the fatigue behavior of such alloy. In early works on Ti-Ni alloys by Melton and Mercier [4,5] it was found that: (i) crack initiation decreases with increasing martensite-start temperature, M_s ; (ii) crackgrowth rates were unaffected by the value of M_s . In fact, they showed that, when dealing with crack growth rate, NiTi in stable martensitic

 $(M_s = 47 \, ^{\circ}\text{C})$ and unstable austenitic $(M_s = 20 \, ^{\circ}\text{C})$ conditions exhibit almost identical response. Similar results were reported in [6] where the fatigue crack resistance of superelastic structure, stable austenite and stable martensite was studied. Results showed that the lower the temperature the higher the fatigue thresholds. Furthermore, they showed that crack-growth rate is slower in stable martensite compared to stable austenite and superelastic austenite. In addition, two values of temperature were used under M_s and, as reported in [4], except for the fatigue threshold, crack propagation did not seem to be affected by the temperature. The effect of the microstructure on the fatigue crack propagation was also investigated in [7] and, also in this work it was found that fatigue-crack growth rates are slowest in the stable (nontransforming) microstructures, particularly the stable austenite, and fastest in the unstable (transforming) microstructures, particularly involving a reversible transformation to martensite. However, it is important to underline that this latter results were achieved by comparing the properties of alloys with different compositions, rather than in the same material as reported in [6]. Fatigue crack growth experiments were also undertaken in [8] with the aim to determine how the fatigue threshold for nickel-titanium alloy with fixed composition changes when the stable martensite and the unstable austenite/stress-induced martensite are investigated. It was found that, as reported in [6], threshold parameter for nickel-titanium increases with decreasing the temperature. In addition, the fatigue crack propagation, in simulated

E-mail address: emanuele.sgambitterra@unical.it (E. Sgambitterra).

^{*} Corresponding author.

body fluid, has been studied in [9–11], by using thin CT specimens directly obtained from flattened NiTi tubes.

Despite this research activity, many aspects of fatigue crack growth in SMAs are still unknown, especially because the stress hysteresis and/or thermally induced phase transformations significantly affect the damage mechanisms occurring under fatigue loadings, i.e. the crack nucleation and propagation mechanisms. An accurate knowledge of these topics is really important for the analysis of the life of damaged structures as well as their failure modes, with the aim to improve the overall performances of NiTi-based components or structures. The fracture behavior of NiTi alloys strongly depends on the microstructure near the crack tip region [12], where marked non-linear phenomena, like phase transformation mechanisms and martensitic variants reorientation are involved. As a direct consequence, classic elastic and/or elastic-plastic theories, with handbook stress intensity calculations to characterize driving forces, cannot be directly applied to SMAs.

For this purpose, proper investigation techniques were recently applied to analyze mechanisms near crack tip, such as synchrotron Xray micro-Diffraction (XRD) [13-15], Infrared thermography (IR) [16,17] and Digital Image Correlation (DIC) [17–23]. In particular, both strain field and lattice evolutions were analyzed by XRD. These studies revealed the occurrence of stress-induced transformation (B2-B19') in austenitic alloys and detwinning/reorientation of B19' structure in martensitic ones. Similar results were obtained by Infrared (IR) thermography that showed direct (B2-B19') and reverse (B19'-B2) crack tip transformations under fatigue loadings, due to the latent heat associated with stress-induced transformations. In addition, DIC was also used to estimate the effective Stress Intensity Factor (SIF) by performing regression on the measured displacement field near the crack tip with the William's series expansion [20-23]. Finally, most recently, nanoindentation technique was proposed as an efficient and easy alternative method to identify near crack tip phase transformations in SMAs [24,25], by using spherical indenters and relatively large indentation loads (400 mN).

Although substantial research has been conducted on the NiTi-based shape memory alloy, most of the work considered the polycrystalline alloys which, nowadays, represent the most commercially applicable. However, it is worth pointing out that single crystal investigations provide more details about the operant deformation mechanisms compared to the polycrystalline NiTi that is usually highly textured [26–28]. Furthermore, using single crystal it is possible to remove grain boundary effects when dealing with fatigue crack growth.

A significant amount of research has been performed on single crystals of Cu-based SMAs even though obtained data cannot be directly transferred to single crystal NiTi due to the different crystal structure and types of transformation that occur in these alloys [29,30].

There are not many studies available on single crystal NiTi; these were focused mainly on mechanical response to uniaxial tension and compression loading conditions [31–33], fracture under uniaxial tension [34,35], the effect of crystallographic orientation on the mechanical behavior [36] and effect of precipitate structure on deformation [37]. Thermally induced martensite was observed in single crystal NiTi, displaying a triangular self-accommodation structure [38]. Most recently, non Schmid behavior was observed in NiTi B2 single crystal and a generalized yield criterion is proposed [39].

However, not many efforts were undertaken in studying the fatigue crack propagation in NiTi single crystal alloys. To this aim, edge-not-ched NiTi samples, with [0 1 2] crystallographic orientation, were investigated in this study. Fatigue tests were performed to evaluate the crack growth rate of the stable austenite and stable martensite structure. Materials with the same composition were used, and so, two different values of temperature were adopted to get the desired microstructure. To evaluate the effective stress intensity factor the sample actually experienced, that can be different from the one predicted by the linear elastic fracture mechanic (LEFM), a proper numerical procedure was implemented. It is based on the regression of the near crack

tip displacements measured by the Digital Image Correlation technique with the William's solution [40]. The procedure is also able to automatically calculate the effective crack length that is different from the physical one if plastic or pseudoplastic deformations occur.

It is important to underline that the proposed approach needs the local elastic properties as input parameter. The mechanical response of SMAs, especially in the martensitic state, is rather complex because the martensite morphology undergoes a transition from a multi-variant ("internally twinned") state to a single variant ("detwinned") arrangement [41,42]. As transition occurs from a multi-variant twinned morphology to a single crystal one, the elastic modulus can increase from 50 GPa to 120 GPa [43] when high deformations are applied. Therefore, which value of the elastic constant has to be used during the crack growth history?

To get an answer, the crack opening displacements were measured by virtual extensometer feature provided by the correlation software. Obtained results were fitted with the analytical solution of the crack opening displacement [44], based on the strip yield model, and the elastic modulus was used as a regression parameter.

Overall, the paper outlines a methodology to characterize the fatigue crack growth where the driving force is represented by the determination of the crack tip displacements. Such procedure provides a wealth of information including the effective stress intensity factor and the automatic localization of the effective crack tip. Furthermore, starting from the crack closure measurements it is also possible to estimate the effective elastic properties near the crack tip. The knowledge of this latter parameter is of great interest especially when dealing with materials that exhibit complex stress induced phenomena near the crack tip, like martensitic variants reorientation.

2. Materials and methods

2.1. Materials and specimens

Single crystal edge-notched Ti-Ni 50.1 at.% samples, with load axis along the [012] crystallographic orientation, were investigated. Each sample was cut by electrical discharge machining (EDM) into a dogbone shape with a hole at each end to facilitate gripping. Fig. 1 displays the geometry of the sample with a visual key to the dimensions.

An edge notch was made at the mid-section of the sample, using EDM with a $0.1\,\mathrm{mm}$ radius wire, to facilitate the formation of fatigue crack.

Each specimen was previously solutionized in order to obtain a solid solution then they were heat treated at 450 °C for 100 h to get a stable martensitic structure at room temperature (T=20 °C) [45]. The characteristic transformation temperatures were obtained by Differential Scanning Calorimetry (DSC) and results are reported in Table 1.

Different isothermal tensile tests were carried out, see Fig. 2a, by monotonically increasing the temperature from 20 °C to 120 °C, to capture the variations of the Young's modulus and critical stress (σ_{cr}). The latter represents the detwinnig stress for the martensitic structure $(T < M_f)$ and B2-B19' transformation stress for the austenitic one $(T > A_f)$. However, it is important to note that for temperature values higher than 80 °C the material exhibited a stable austenitic behavior, i.e. without phase transformation and pseudoelastic recovery capability. As shown in Fig. 2, the material exhibits a typical martensitic response in the temperature range 20-40 °C, with almost constant Young's modulus ($E_M \approx 40 \text{ GPa}$) [46] and detwinning stress $(\sigma_{cr} \approx 150 \text{ MPa})$. A pseudoelastic behavior was observed in the temperature range 50-60 °C with a Young's modulus approaching the austenitic one and a critical stress increasing with the temperature. A typical austenitic response, with no recovery capability, was observed at higher temperatures ($T \ge 80$ °C), with the constant elastic modulus $(E_A \approx 80 \text{ GPa})$ and a critical stress almost constant with the temperature ($\sigma_{cr} \approx 550$ MPa). In this study, two values of the temperature were investigated, i.e. T = 20 °C and T = 80 °C, in order analyze the fatigue

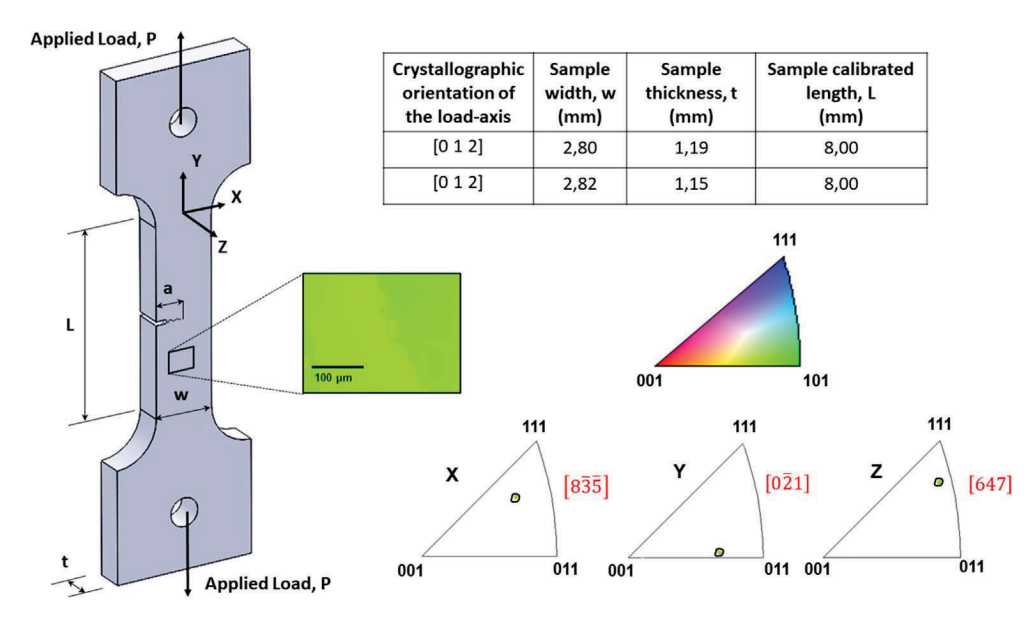


Fig. 1. Visualization of the investigated sample.

Table 1Transformation temperatures of the investigated material (°C).

$A_{\scriptscriptstyle S}$	A_f	$M_{\scriptscriptstyle S}$	M_f
45	55	30	25

crack growth response of the two stable crystallographic phases of the material. Crystallographic orientation of the samples was determined by electron backscattered diffraction (EBSD) at T=20 °C and by X ray diffraction (XRD) at T=80 °C. In both cases, it was seen that the load axis direction is [0 1 2], the width direction is [8 $\overline{3}$ $\overline{5}$] whereas the thickness direction is [6 4 7], see Fig. 1.

2.2. Fatigue tests

Load controlled fatigue tests were performed, by using a servo-hydraulic testing machine equipped with a load cell of 10 kN, applying a maximum stress $\sigma_{max} = 60$ MPa, a fixed stress ratio $(R = \sigma_{min}/\sigma_{max} = 0.1)$ and a frequency of 5 Hz,. Most recently, it was

demonstrated that crack growth rate is significantly dependent on the loading frequency in SMA when dealing with pseudoleastic alloy [47]. In fact, due to the thermo-mechanical coupling effect, a decreasing of the crack growth rate with increasing the frequency was obtained. However, no phase transformations are involved on the investigated samples, therefore no effect of the frequency, on the fatigue crack growth, should be expected.

The specimens were polished to a mirror finish. Black paint was then airbrushed to create a speckle pattern on the specimen surface for the digital image correlation (DIC) analysis.

A commercial image correlation program (Vic-2D, Correlated Solutions, USA) was used to perform DIC analysis. A digital camera was adopted to capture images during the fatigue crack growth experiments. The camera resolution was 1600 by 1200 pixels, the maximum frame rate was 15 fps, and an adjustable lens with a 12X magnification range and 2X adapter was used. The experimental setup is shown in Fig. 3.

A computer program controls the load frame and synchronizes the acquisition of the images. Once a crack was visually identified, measurement cycles were run periodically, at 0.25 Hz, to capture a

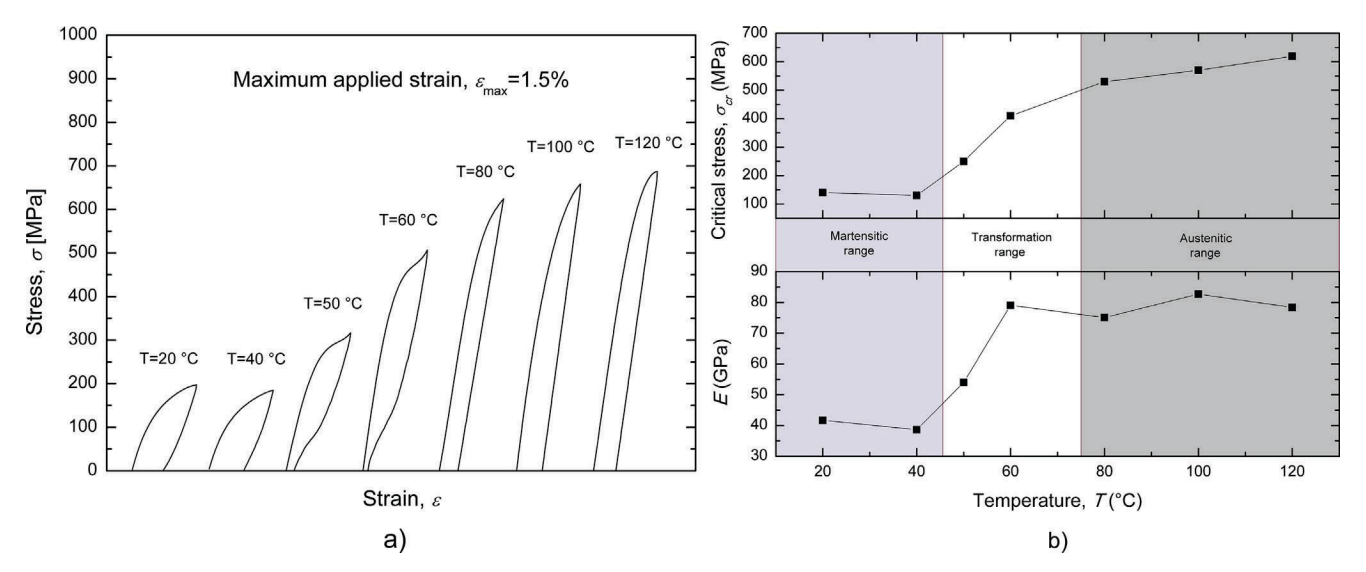


Fig. 2. Mechanical properties of the material (Ti-Ni 50.1 at. %) along the [0 1 2] orientation as a function of the testing temperature in the range 20–180 °C: (a) isothermal stress-strain curves and (b) elastic modulus and critical stress.

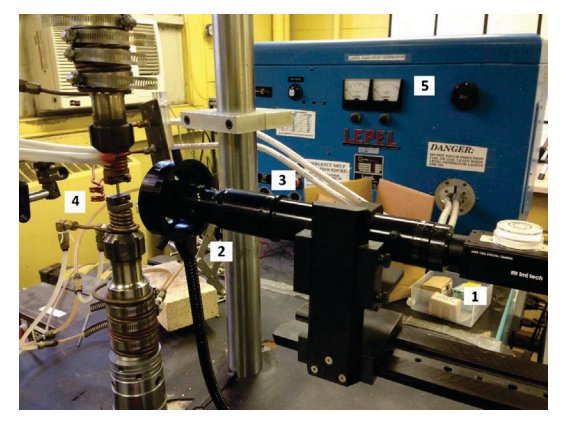


Fig. 3. The experimental setup. Labeled in the figure: (1) camera, (2) light source, (3) lens, (4) specimen, and (5) thermal induction equipment.

significant number of images to provide an in-depth analysis into the fatigue cycles.

The first image of each measurement cycle, captured at minimum load, was used as the reference for DIC analysis. The maximum subset size was 85 μ m by 85 μ m with a maximum of 8 μ m between the centers of the subsets. The DIC allowed determination of both the horizontal (u_x) and vertical (u_y) displacements (see Fig. 4). In particular, the displacement vector for a grid of m measurements points around the crack tip, namely $\{u^*\} = \{u_{x1}, u_{y1}, \cdots, u_{xi}, u_{yi}, \cdots, u_{xm}, u_{ym}\}$, were captured to estimate the effective stress intensity factor by the least square regression of DIC data, as described in the following sections.

Fatigue crack propagations curves $(da/dN \ vs \ \Delta K)$ were obtained, based on Mode I stress intensity range estimated by least square regressions. In fact, almost straight cracks perpendicular to the load axis were always observed and a negligible mode mixity was recorded $(K_{II}/K_{I} < 0.05)$. It is worth noting that crack closure effects, which usually happen during crack propagation experiments, result in a reduced actual stress intensity range. In particular, crack opening occurs at the opening SIF (K_{op}) , which could be slightly higher than the applied minimum one (K_{min}) , and the effective stress intensity range must be calculated accordingly ($\Delta K_e = K_{max} - K_{op}$). This is normally carried out by capturing the crack opening load during fatigue cycling. However, DIC method directly provides the actual stress intensity range, as it is based on the real near crack-tip displacement field experienced by the sample during fatigue loading, i.e. no crack opening is recorded for $K < K_{op}$ and ΔK accounts for the contribution only when the crack is fully open.

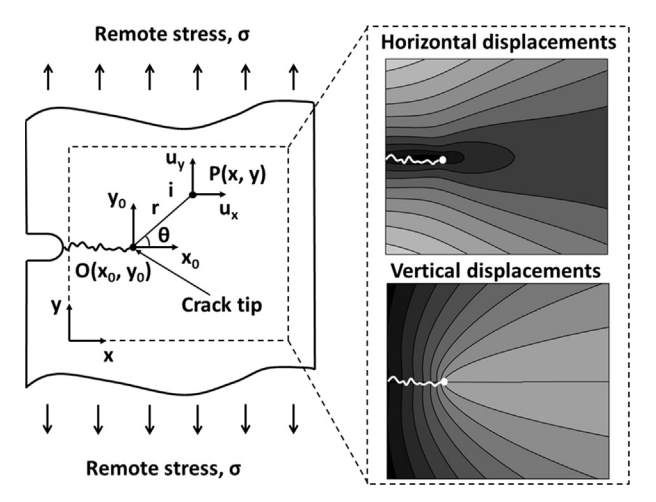


Fig. 4. Schematic depiction of a single edge crack subjected to a remote stress, together with the corresponding near crack tip horizontal and vertical displacements.

2.3. SIF estimation by linear regression analysis

To determine the effective stress intensity factor, the specimen actually experiences, a least squares regression was performed on the DIC measured displacements, by the William's expansion series [40]. In fact, theoretical methods, based on linear elasticity, do not consider the large crack-tip nonlinearities occurring in SMAs and, consequently, do not provide correct estimation of the SIF. The near crack-tip displacement field $\{u\} = \{u_x \ u_y\}^T$ based on William's expansion series, as a function of the polar coordinate with origin at the crack tip (r,θ) , for an anisotropic material is given by [40]:

$$\{\boldsymbol{u}\} = \{u_x \quad u_y\}^T = \begin{bmatrix} \psi_{11} & \psi_{12} \\ \psi_{21} & \psi_{22} \end{bmatrix} \{K_I \quad K_{II}\}^T$$
(1)

where K_I and K_{II} are the mode I and mode II stress intensity factors, respectively; ψ_{ij} are functions of the polar coordinates (r,θ) and are given by:

$$\begin{aligned} \psi_{11} &= \sqrt{\frac{2r}{\pi}} \operatorname{Re} \left[\frac{1}{\mu_1 - \mu_2} \{ \mu_1 p_2 \sqrt{\cos\theta + \mu_2 \sin\theta} - \mu_2 p_1 \sqrt{\cos\theta + \mu_1 \sin\theta} \} \right] \\ \psi_{12} &= \sqrt{\frac{2r}{\pi}} \operatorname{Re} \left[\frac{1}{\mu_1 - \mu_2} \{ p_2 \sqrt{\cos\theta + \mu_2 \sin\theta} - p_1 \sqrt{\cos\theta + \mu_1 \sin\theta} \} \right] \\ \psi_{21} &= \sqrt{\frac{2r}{\pi}} \operatorname{Re} \left[\frac{1}{\mu_1 - \mu_2} \{ \mu_1 q_2 \sqrt{\cos\theta + \mu_2 \sin\theta} - \mu_2 q_1 \sqrt{\cos\theta + \mu_1 \sin\theta} \} \right] \\ \psi_{22} &= \sqrt{\frac{2r}{\pi}} \operatorname{Re} \left[\frac{1}{\mu_1 - \mu_2} \{ q_2 \sqrt{\cos\theta + \mu_2 \sin\theta} - q_1 \sqrt{\cos\theta + \mu_1 \sin\theta} \} \right] \end{aligned}$$

$$\left(2 \right)$$

where Re denotes the real part of a complex number, while p_k and q_k are given by:

$$\begin{cases} p_k = a_{11}\mu_k^2 + a_{12} - a_{16}\mu_k \\ q_k = a_{12}\mu_k + \frac{a_{22}}{\mu_k} - a_{26} \end{cases}$$
(3)

 μ_k are the complex roots of the characteristic Eq. (4):

$$a_{11}\mu^4 - 2a_{16}\mu^3 + (2a_{12} + a_{66})\mu^2 - 2a_{26}\mu + a_{22} = 0$$
(4)

 a_{ij} are the components of the elastic compliance matrix [C]:

$$\{\varepsilon\} = [C]\{\sigma\} \tag{5}$$

where $\{\varepsilon\}$ and $\{\sigma\}$ are the strain and stress vectors, respectively.

As the samples are subjected to rigid body motions during the experiments, three in-plane rigid motion terms, i.e. rotation (A) and rigid translation perpendicular (B_x) and parallel (B_y) to the load axis have to be included into Eq. (1). Furthermore, the T-stress term (T), i.e. the second term of the William's series, is taken into account in order to improve the fitting between analytical and experimental results, as follows:

$$\{\boldsymbol{u}\} = [\boldsymbol{\psi}]\{\boldsymbol{U}\}$$

$$= \begin{bmatrix} \psi_{11} & \psi_{12} & \psi_{13} & \psi_{14} & \psi_{15} & \psi_{16} \\ \psi_{21} & \psi_{22} & \psi_{23} & \psi_{24} & \psi_{25} & \psi_{26} \end{bmatrix} \{K_{I} \quad K_{II} \quad T \quad A \quad B_{x} \quad B_{y}\}^{T}$$
(6)

where $\{U\} = \{K_I \quad K_{II} \quad T \quad A \quad B_x \quad B_y\}^T$ represents the vector of unknown parameters and the additional functions ψ_{ij} are given by:

$$\begin{aligned} & \psi_{13} = r \ a_{11} \cos\theta \\ & \psi_{14} = -r \ \sin\theta \\ & \psi_{15} = \psi_{26} = 1 \\ & \psi_{16} = \psi_{25} = 0 \\ & \psi_{23} = -r \ \nu \ a_{12} \sin\theta \\ & \psi_{24} = r \cos\theta \end{aligned}$$
 (7)

Eq. (6) can be also rewritten as a function of the Cartesian coordinates (x, y) (see Fig. 4) by the following substitutions:

$$\begin{cases} r = \sqrt{(x - x_0)^2 + (y - y_0)^2} \\ \theta = \tan^{-1}((y - y_0)/(x - x_0)) \end{cases}$$
 (8)

where (x_0,y_0) are the coordinates of the crack tip (see Fig. 4). If Eq. (6) is applied to the m measurements points of the DIC the following system of 2m linear equations is obtained:

$$\{\boldsymbol{u}^*\} = [\boldsymbol{\psi}^*]\{\boldsymbol{U}\} \tag{9}$$

where $[\psi^*]$ is a 2mx6 matrix obtained by computing the matrix $[\psi]$ of Eq. (6) in the m measurement points. Eq. (9) represents an overdetermined system of linear equations, i.e. with 6 unknowns and 2m equations. In such cases the least square method can be used, which minimizes the sum of the squares of the errors, by the pseudo-inverse of the matrix $[\psi^*]$:

$$\{U\} = ([\psi^*]^T [\psi^*])^{-1} [\psi^*]^T \{u^*\}$$
(10)

2.4. Effective SIF estimation by non-linear regression analysis

The knowledge of the crack tip location is required to apply the method described in the previous section. Usually, the physical location is identified by the digital images captured during fatigue testing. The corresponding coordinates (x_0,y_0) are used for the linear fitting described previously. However, such physical location does not give the best fit of the linear solution of Eq. (9), as the crack-tip nonlinearities cause a redistribution of the linear stress and displacement fields. In particular, in standard elastic-plastic metals, the vertical asymptote of the crack-tip stress is moved by a quantity Δa , that is proportional to the extent of the plastic zone $(\Delta a \propto (K_I/S_Y)^2)$, resulting in an effective crack-tip length and SIF, namely a_e and K_{Ie} , as described by the Irwin correction of the LEFM. As a consequence, estimation errors on the SIF are expected if physical crack-tip location is used instead of the effective one.

This phenomenon was also analyzed in fracture mechanics of SMAs [23], where the SIF was computed based on crack length corrections similar to the Irwin's approach for elastic-plastic materials. It was shown that these effects are even more important in SMAs due to the marked crack-tip non-linearity resulting from local stress-induced transformations. In particular, small estimation errors are expected under the assumption of small scale transformation, as discussed in [48–52], i.e. for low values of the SIF. When increasing the SIF, crack-tip non-linearity cannot be neglected and the effective crack length has to be considered.

To overcome this limitation the effective crack tip coordinates, namely (x_e, y_e) , must be considered as unknown parameters in Eq. (6), i.e. they have to be included in a new vector of unknowns $\{U\} = \{K_I \quad K_{II} \quad T \quad A \quad B_x \quad B_y \quad x_e \quad y_e\}^T$. However, this leads to a system of non-linear equations and, consequently, a new non-linear fitting procedure was developed.

In particular, the vector of unknown parameters $\{U\}$ is calculated by an iterative procedure based on Newton-Raphson method. To this aim Eq. (6) can be written as a series of iterative equations based on Taylor's series expansions as follows:

$$\{\boldsymbol{u}\}_{n+1} = \{\boldsymbol{u}\}_n + \sum_{j=1}^{8} \left[\frac{\partial \{\boldsymbol{u}\}}{\partial U_j} \Delta U_j \right]_n = \{\boldsymbol{u}\}_n + \nabla \{\boldsymbol{u}\}_n \{\Delta \boldsymbol{U}\}_n$$
(11)

where the subscript n indicates the n-th iteration step, $\nabla\{u\}$ is the gradient (2 × 8 matrix) with respect to the unknown terms $\{U\}$ and $\{\Delta U\} = \{\Delta K_I \ \Delta K_{II} \ \Delta T \ \Delta A \ \Delta B_x \ \Delta B_y \ \Delta x_e \ \Delta y_e\}^T$ is the correction to the estimation of the vector $\{U\}$ at the n-th step.

Eq. (11) can be rewritten in terms of the correction of the displacement vector at the *n*-th step, namely $\{\Delta \mathbf{u}\}_n = \{\mathbf{u}\}_{n+1} - \{\mathbf{u}\}_n$:

$$\{\Delta \mathbf{u}\}_n = [\xi]_n \{\Delta \mathbf{U}\}_n \tag{12}$$

where the matrix $[\xi]_n$ (2 × 8) represents the gradient of the

displacement vector $\{u\}_n$ (see Eq. (11)).

If Eq. (11) is applied to the m measurements points and the displacement vector at the n+1 step is set to the experimental one $(\{\Delta u^*\}_n = \{u^*\} - \{u\}_n)$ the following overestimated system of 2m equations is obtained:

$$\{\Delta \mathbf{u}^*\}_n = [\boldsymbol{\xi}^*]_n \{\Delta U\}_n \tag{13}$$

where $[\xi^*]_n$ is a 2mx8 matrix obtained by computing the matrix $[\xi]_n$ of Eq. (11) in the m points.

Least squares regression gives the best fit of $\{\Delta U\}_n$:

$$\{\Delta U\}_n = ([\xi^*]_n^T [\xi^*]_n)^{-1} [\xi^*]_n^T \{\Delta u^*\}_n$$
(14)

The solution of the system gives the correction vector of unknowns for prior estimates of the coefficients. Accordingly, an iterative procedure must be used to obtain the best-fit set of coefficients. The procedure described above is repeated until the corrections $\{\Delta U\}$ become acceptably small.

It is important to point out that convergence cannot be easily reached if the initial trial values for $\{\Delta U\}$ are far from the effective ones. However, it was observed that if the trial location of the crack tip is not far from the real one, convergence of the solution is quite fast.

To validate the new fitting procedure, finite element (FE) simulations were carried out. In particular, an elastic-plastic material was modeled with the same Young's modulus of martensitic SMA ($E=40~\mathrm{GPa}$) and with the yield stress equal to the detwinning stress of the SMA ($S_y=150~\mathrm{MPa}$). In fact, this leads to a very similar size of the crack-tip non-linear zone and, consequently, to a comparable variation in the effective crack-tip length and SIF. In addition, this test case represents the worst condition among the investigated ones, as it has the lowest critical stress and, consequently, the largest non-linear zone.

The specimen in Fig. 1 was modeled by 2D four-node shell elements and a special refinement was adopted for the near crack tip zone. Pure Mode I loading was applied, by a concentrated load P at the pinhole (see Fig. 5a). Nodal displacements were considered as the target solution for least square regression, i.e. they are related to the experimental displacement $\{u^*\}$. Eq. (10) were firstly used to fit the numerical data obtained from the simulations, i.e. by considering the physical location of the crack tip. In Fig. 5b the contours of the vertical displacement near the crack tip obtained from FE simulations (blue contours) are compared with those given by the linear regression method (red contours). Results show that if plasticity occurs, due to the high stress localization, the numerical displacements do not match with the analytical ones, affecting the calculation of the fracture parameters. On the contrary when the effective crack tip is well identified, by the non-linear fitting described above (Eq. (14)), a much better agreement between the two solutions is observed, as shown in Fig. 5c.

2.5. Crack opening displacement measurements

Virtual extensometers, a tool provided by the DIC method, were used to measure the Crack Opening Displacement (COD). Basically, they track two subsets, one on each side of the crack, as shown in Fig. 6. Since the virtual extensometers require no physical setup, many of these can be placed along the crack line, as shown in Fig. 6a. In particular, virtual extensometers, provide the displacement components parallel (u_y) and perpendicular to the load axis (u_x) . The differences in the displacement components between the two sides of the crack, namely $\delta_I = u_{y,up} - u_{y,low}$ and $\delta_I = u_{x,up} - u_{x,low}$ are obtained accordingly (see Fig. 6c). The parameter δ_I and δ_{II} describes the opening (Mode I) and sliding (Mode II) modes, respectively.

It is important to underline that, due to closure mechanisms, crack flanks will result close when the applied load, P, is lower than the value required to completely open the crack, P_{op} , see the blue dashed crack profile in Fig. 6c. At this stage $K_I < K_{op}$ therefore no SIF will be recorded by the regression analysis. Only when $P \geqslant P_{op}$ crack tip will be completely open, see the dark bold profile of the crack in Fig. 6c. At this

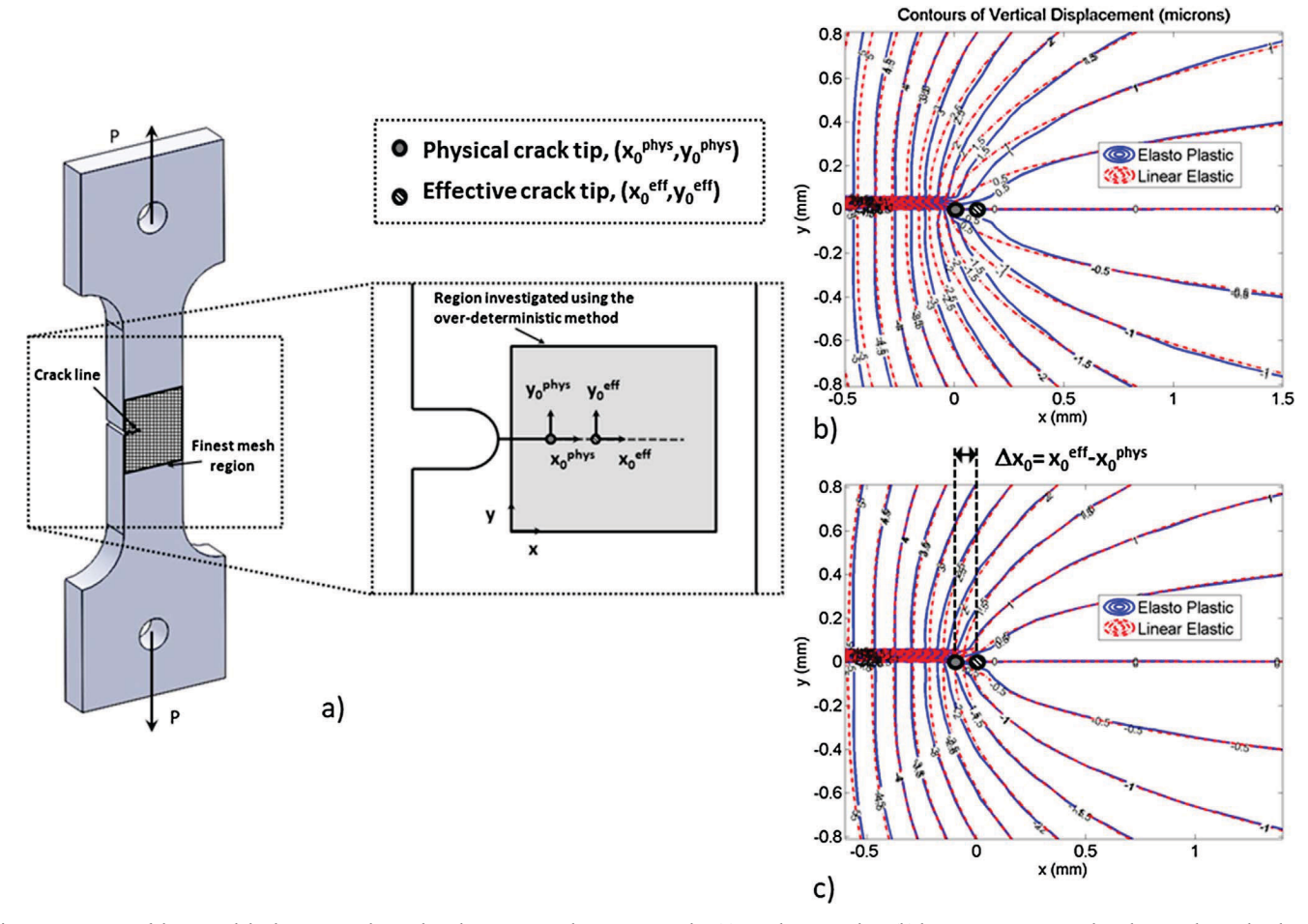


Fig. 5. Comparison of the vertical displacement at the crack tip between FE and regression results: (a) correlation window; (b) linear regression carried out by considering the physical location of the crack tip; (c) non-linear regression carried out by estimating the effective crack tip.

stage $K_I \geqslant K_{op}$ and an appreciable SIFs will be recorded by the regression analysis.

To measure the COD virtual extensometers with subset size of 21 by 21 pixels were used in this study and the first image of each loading cycle was taken as the reference image for digital correlation.

The extensometers were equally spaced, at a distance of about $15\,\mu m$ for small crack length and $50\,\mu m$ for bigger size, along the crack line, from the EDM notch to the crack tip. The COD profile during loading was directly obtained by this method.

3. Results and discussion

3.1. Near crack-tip displacements

To demonstrate the accuracy of the non-linear regression technique, the experimental and regressed displacement fields were systematically compared. Computations were carried out by considering isotropic properties for the martensitic structure (B19'), i.e. the following inplane elastic compliance coefficients were used:

$$\begin{cases} a_{11} = a_{22} = 1/E \\ a_{12} = -\nu/E \\ a_{16} = a_{26} = 0 \\ a_{66} = 1/G \end{cases}$$
(15)

where E and v represent the Young's modulus and Poisson's ratio, respectively, while and G = E/(2(1+v)) is the shear modulus. In fact, this simplified assumption has been proved in [53], where it has been demonstrated that the material exhibits similar behavior in different

orientations. In addition, the presence of randomly oriented martensitic variants gives almost isotropic properties in B19′. On the contrary, anisotropic properties were set for the austenite (B2) according to the values reported in [53].

Fig. 7 report the displacement contours obtained from the austenitic (B2) and martensitic (B19') specimens for a crack length a=1.12 mm at the maximum applied stress $\sigma_{max}=60$ MPa. In particular, Fig. 7a and b report the vertical and horizontal displacements, respectively, for austenite (B2), whereas Fig. 7c and d show the vertical and horizontal displacements for martensite (B19'). The blue and red contours represent the experimental and regressed results, respectively. A good agreement between experiments and computations is observed.

In addition, a little inclined path was observed during the crack propagation (see Fig. 7a and c), but the maximum inclination angle is 7° and the mode II stress intensity range (ΔK_{II}) is one order of magnitude lower than that of mode I (ΔK_{I}). For this reason, the effect of mode II was neglected in this study.

3.2. Fatigue crack propagation

Fatigue crack propagations curves $(da/dN \ vs \ \Delta K)$ were obtained, based on mode one effective stress intensity range (ΔK_{Ie}) estimated by the non-linear regression method described in Section 2.4. Effective stress intensity ranges were compared with those obtained by Linear Elastic Fracture Mechanics (LEFM), namely ΔK_{ILE} :

$$\Delta K_{ILE} = \Delta \sigma \sqrt{\pi a} \cdot f\left(\frac{a}{w}\right) \tag{16}$$

where $\Delta \sigma$ is the remote stress range and $f(\frac{a}{w})$ is the geometric factor for

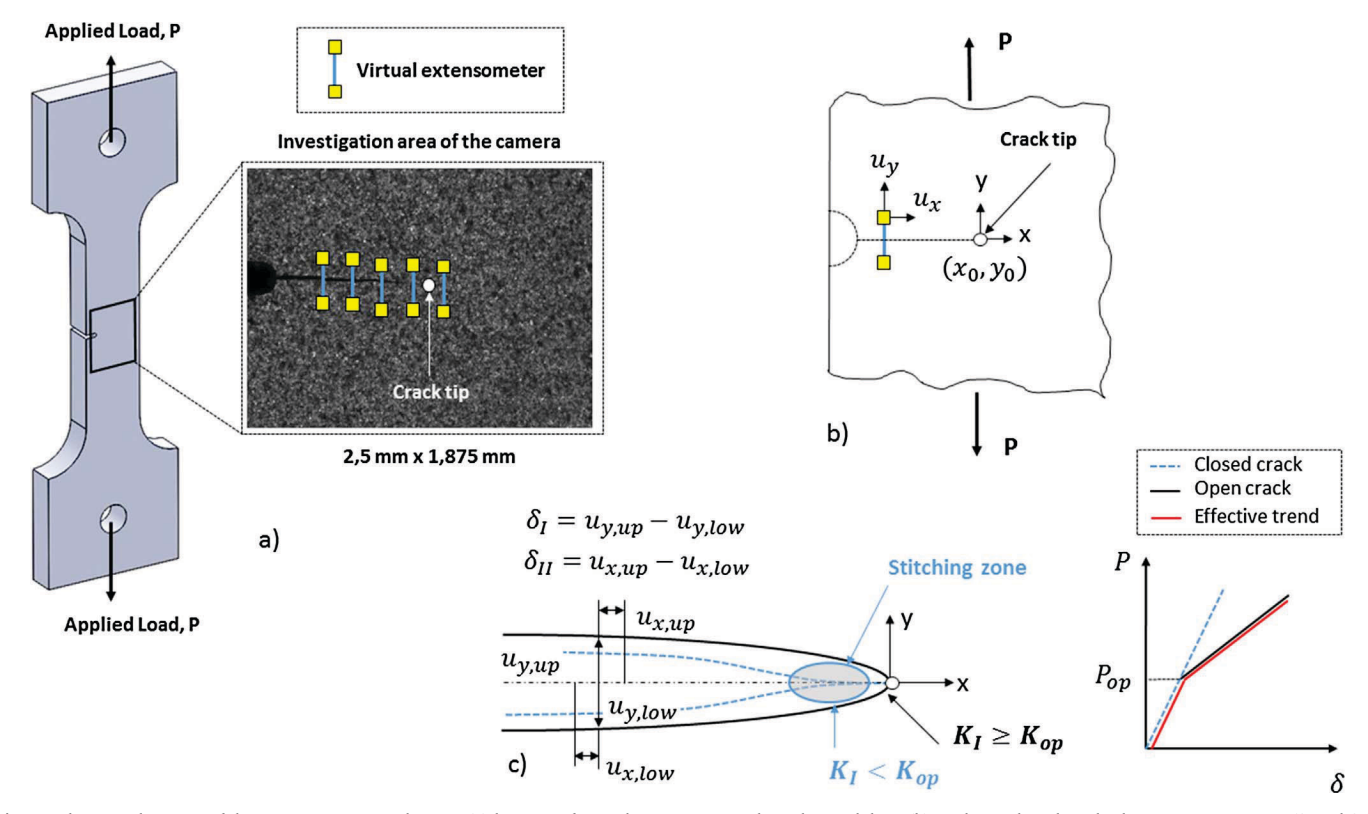


Fig. 6. Schematic depiction of the COD measurement by DIC: (a) location of virtual extensometers along the crack line; (b) mode I and mode II displacement components (δ_I and δ_{II}).

a single-edge notch tension specimen [54]:

$$f\left(\frac{a}{w}\right) = 1.12 - 0.23\left(\frac{a}{w}\right) + 10.55 \cdot \left(\frac{a}{w}\right)^2 - 21.71 \cdot \left(\frac{a}{w}\right)^3 + 30.38 \cdot \left(\frac{a}{w}\right)^4$$
(17)

Crack propagation curves for both martensitic (B19') and austenitic structures (B2) are reported in Fig. 8a and b, respectively. Obtained data show higher scattering in the austenitic curve compared to the martensitic one. This effect can be attributed to the different displacement amplitude experienced by the two microstructures. In fact, if the contour plots, reported in Fig. 7, are compared, it is possible to observe that austenite experiences lower amplitude, as a consequence of its higher stiffness, compared to the twinned martensite. This results in higher noise of the austenitic displacement maps, see Fig. 7, and higher dispersion of the SIF data when they are calculated with the regression method. Figures also reports a direct comparison between effective data, obtained from DIC, and LEFM predictions. In addition, data within the steady state crack propagation regime, were fitted to the Paris law:

$$\frac{da}{dN} = C(\Delta K_I)^m \tag{18}$$

The values of the coefficients (C and m), for both effective and LEFM data, are also reported in Fig. 8. Comparison between Fig. 8a and b shows higher values of the exponent m for the martensitic phase, resulting in a higher propagation rate. In addition, marked differences between effective and LEFM data are highlighted, with significantly lower values of the exponent m in the LEFM curves. In particular, m decreases from 3.1 to 1.6 for B19′ and from 2.8 to 1.2 for B2 structure. The differences between the two methods are attributed to both the crack closure effects and the near crack tip fields redistribution, caused by local large non-linearity including both phase transitions and plasticity. In fact, these effects are taken into account by the DIC method, as described in the previous sections, instead they are neglected by LEFM. In addition, the values of m obtained by LEFM are considerably smaller than typical values for engineering alloys, which are in the range

m = 2-7 [55].

Furthermore, the figures also show the differences in the fatigue threshold ($\Delta K_{I,th}$) measured using the two methods. In particular, concerning the B19′ structure the LEFM fatigue threshold was determined to be $\Delta K_{ILE,th}=4$ MPa· m^{1/2} whereas the effective one was $\Delta K_{Ie,th}=3.3$ MPa·m^{1/2}. For the B2 structure, instead, the LEFM fatigue threshold was determined to be $\Delta K_{ILE,th}=3.7$ MPa·m^{1/2} whereas the effective one was $\Delta K_{Ie,th}=1.4$ MPa·m^{1/2}. Obtained data revealed that more evident closure mechanisms occur when dealing with the austenitic microstructure.

Fig. 9 reports a direct comparison of the effective curves for the two crystallographic phases. Both structures show a comparable behavior in the Paris regime with a slope m=3.1 for the B19′ and m=2.8 for the B2 microstructure. On the contrary, they behave in a drastically different way in the near threshold zone. In fact, effective fatigue thresholds were determined to be $1.4 \, \mathrm{MPa} \cdot \mathrm{m}^{1/2}$ for B2 and $3.3 \, \mathrm{MPa} \cdot \mathrm{m}^{1/2}$ for B19′ microstructure. The latter result is in agreement with data reported in [6], where the crack propagation in NiTi shape memory alloys, considering closure mechanisms, was studied. In addition, in [56], where only the martensitic structure was analyzed, even higher values of $\Delta K_{I,th}$ with respect to our study was recorded.

On the contrary, a different trend was observed in [7], where higher values of threshold were found for austenite than martensite. However, it is important to underline that in this literature work the LEFM approach was adopted.

Table 2 shows a direct comparison between literature results and those obtained in this work.

It is worth noting that data presented in this paper are very valuable because they draw attention to the precise measurements near threshold. In addition, obtained results are based on experiments performed on single crystal alloy, i.e. without grain boundaries, and, therefore, they reflect an intrinsic measure of the threshold. The addition of grain boundaries, in fact, will contribute to irreversibility which in turn accelerates crack growth [57]. In this study grain boundary effects are removed while focusing on the intrinsic matrix fatigue crack

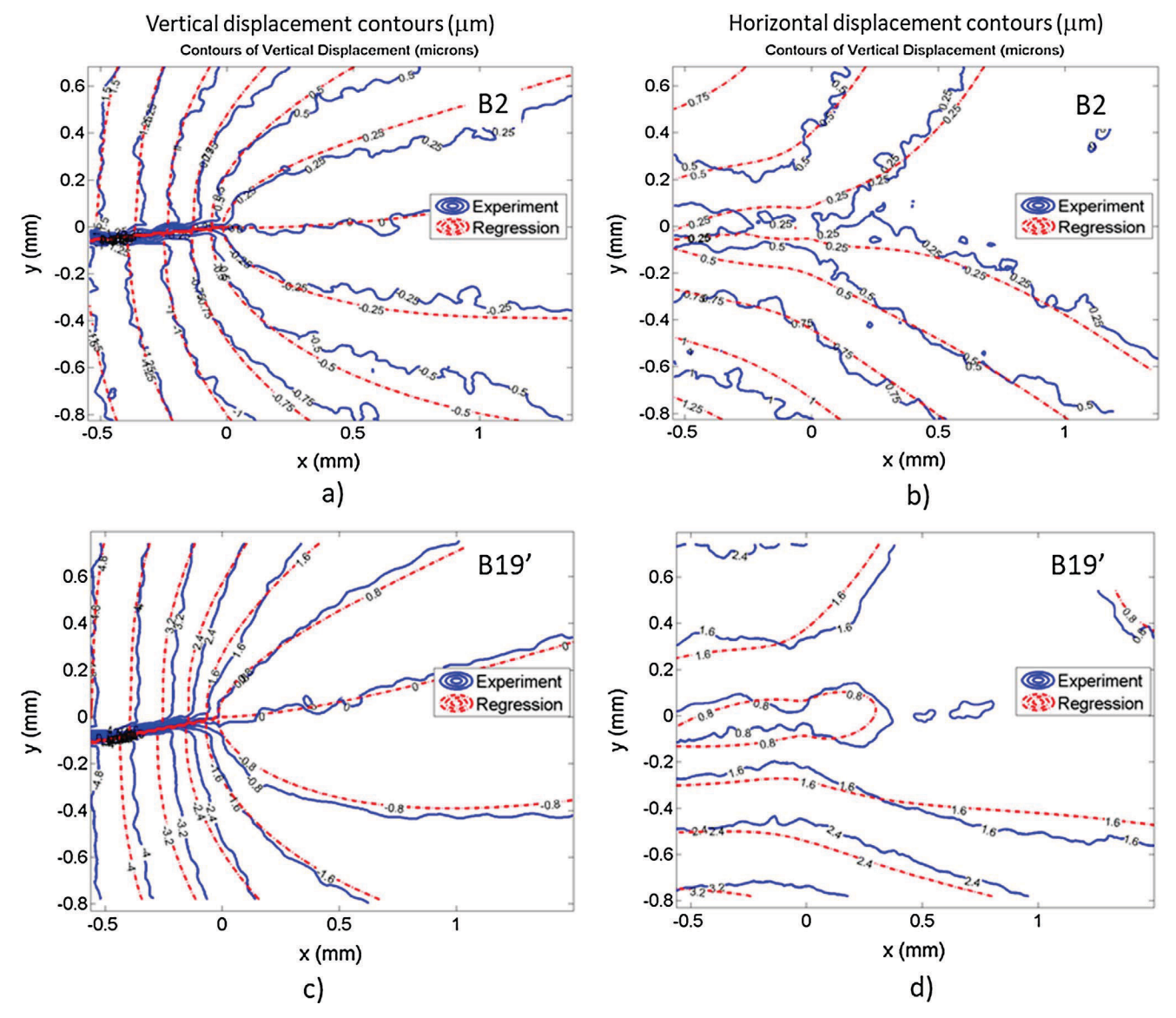


Fig. 7. Comparison between experimentally measured and regressed displacement contours for a crack length a=1,12 mm at the maximum applied stress $\sigma_{max}=60$ MPa: a) vertical displacements for austenite (B2); b) horizontal displacements for martensite (B19'); d) horizontal displacements for martensite (B19').

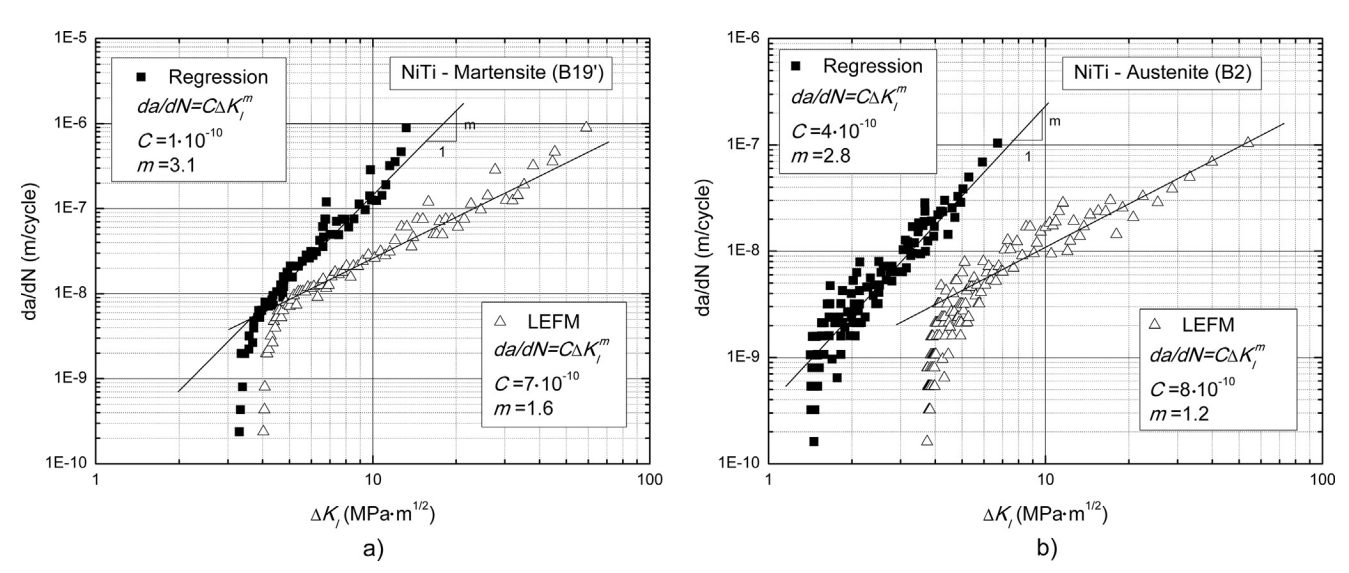


Fig. 8. Crack propagation behavior calculated using the digital image correlation (DIC) and the linear elastic fracture mechanics (LEFM): (a) martensitic structure; (b) austenitic structure.

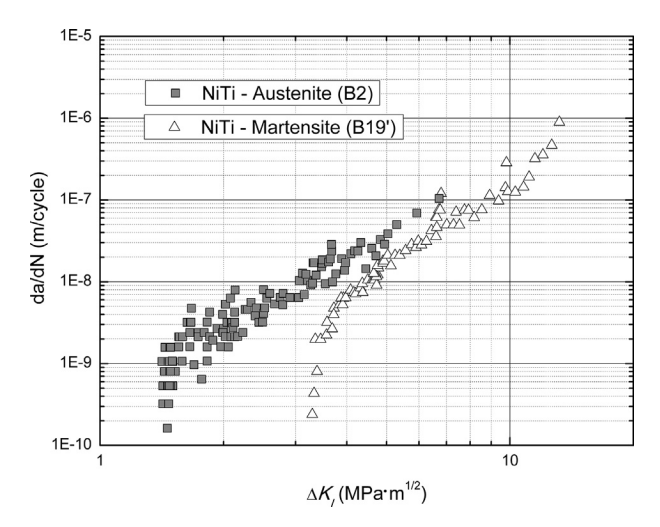


Fig. 9. Comparison between the crack propagation behavior of austenitic and martensitic structures.

growth response.

3.3. Crack opening displacements

DIC displacement gages were used to measure crack opening displacements (δ_l) along the crack length. Figs. 10 and 11 show the crack opening displacement for increasing values of the applied load. Data are normalized with respect to the maximum opening displacement (δ_{lmax}^*) recorded by the closest virtual extensometer to the notch, at the maximum load P_{max} .

Results are reported for the austenitic (Fig. 10) and martensitic (Fig. 11) microstructures, and for two different values of the crack length (a = 1.2 mm in Figs. 10a and 11a, a = 1.75 mm in Figs. 10b and 11b)

As shown in Fig. 10, the austenitic structure exhibited clear closure mechanisms, in fact crack flanks, behind the crack tip, result closed up when the load is lower than around 20% of the peak one, $P_{op} \approx 0.2 \cdot P_{max}$. Only when $P \geqslant P_{op}$ crack tip appears to be completely open. It is important to note that no clear results were obtained for the shortest crack sizes due to the numerical noise related to the low resolution of the pictures, however no closure should be expected during this time.

On the contrary, no evident closure effect was observed in the martensitic specimen, where the crack seems to be always open until a length a=1.8 mm, after that it appears close up to around 5% of peak load, $P_{op}\approx 0.05 \cdot P_{max}$.

This latter result seems to not completely agree with the crack propagation behavior exhibited by the martensitic structure shown in Fig. 8. In fact, near the threshold regime the LEFM and effective curves almost match, confirming that closure effects do not play an important role. On the contrary, in the Paris and critical regime their trend is completely different and closure mechanisms should be expected. The

observed behavior can be related to the particular microstructure of the martensitic material near the crack tip. In fact, it is well known that martensite is characterized by a random distribution of variants whose orientation can significantly affect the elastic properties [46]. Typically, their orientation is related to the direction of the applied load, in fact they tend to align with it and the higher the stress level the closer the martensitic orientation with respect to the loading axis. However, these mechanisms are closely related to the crack length, as the shorter the crack the smaller the volume of material subjected to stress induced transitions. As a consequence, during the first stage of the fatigue life, no evident reorientation mechanisms should be expected close to the crack tip and no big change on the local elastic properties should occur. When crack gets longer, a bigger volume of material will experience high stress and a higher number of variants will reorient in the most favorable applied stress direction, increasing the local stiffness of the material. Fig. 12 qualitatively depicts this phenomenon.

In particular, figure shows that at the first cycle (stress free condition) the near crack tip variants are randomly distributed and the elastic properties recorded from the monotonic tensile test, Fig. 1, should be expected. When the crack starts to propagate it will grow in a new structure characterized by partially distributed variants with higher stiffness. At the end of the its life, the crack should be totally surrounded by a new structure with almost completely distributed variants and with the highest stiffness experienced by the sample [43].

In order to better investigate on this phenomenon, crack tip opening displacement range was used as a physically measurable fracture mechanic parameter to characterize crack growth. In particular, analytical solution of the maximum crack tip opening displacement (δ_{lmax}), based on the strip yield model, was used to fit the experimental data [44]:

$$\delta_{lmax} = \frac{(K_{lmax})^2}{E\sigma_{cr}} \left[\left(1 - \frac{x}{w} \right)^{0.5} - \frac{x}{w} ln \left| \frac{1 + (1 - \frac{x}{w})^{0.5}}{1 - (1 - \frac{x}{w})^{0.5}} \right| \right]$$
(19)

where $K_{I\max}$ is the SIF obtained at the maximum load (P_{\max}) , σ_{cr} is the critical stress and w is the maximum extent of the non-linear zone (detwinning and plasticity) given by:

$$w = \frac{\pi}{8} \left(\frac{K_{\text{Imax}}}{\sigma_{cr}} \right)^2 \tag{20}$$

Upon unloading to $P_u = 0.8 \cdot P_{\text{max}}$, leading to a SIF K_{Iu} , the crack tip opening displacement changes as follows:

$$\Delta \delta_{I} = \delta_{Imax} - \delta_{Iu} = \frac{(K_{Imax} - K_{Iu})^{2}}{2E\sigma_{cr}} \left[\left(1 - \frac{x}{\Delta w} \right)^{0.5} - \frac{x}{2\Delta w} ln \left[\frac{1 + \left(1 - \frac{x}{\Delta w} \right)^{0.5}}{1 - \left(1 - \frac{x}{\Delta w} \right)^{0.5}} \right] \right]$$
(21)

where Δw is equal to:

$$\Delta w = \frac{\pi}{32} \left(\frac{K_{I \max} - K_{Iu}}{\sigma_{cr}} \right)^2 \tag{22}$$

The SIF variation upon unloading ($K_{Imax}-K_{Iu}$), in Eq. (21) is directly

Table 2Paris law parameters obtained from literature and from this study.

Reference	$\Delta K_{th} [\mathrm{MPa} \cdot \mathrm{m}^{1/2}]$		$C [(m/\text{cycle})/(\text{MPa·m}^{1/2})^m]$		m	
	Austenite	Martensite	Austenite	Martensite	Austenite	Martensite
[4]		2.4 (LEFM)		5·10 ⁻¹¹		2.6
[6]	2.5 (LEFM) 1.8 (Effective)	3 (LEFM)	7.10^{-11}	3.10^{-12}	3.3	3.8
[7] [8] [56]	5.4 (LEFM)	4.5 (LEFM) 3.5 (LEFM) 5.8 (LEFM)	3·10 ⁻¹²	8.10^{-12} 2.10^{-12} 3.10^{-13}	2.8	3.1 4 4.6
Present results	3.7 (LEFM) 1.4 (Effective)	4 (LEFM) 3.3 (Effective)	8·10 ⁻¹⁰ (LEFM) 4·10 ⁻¹⁰ (Effective)	7.10^{-10} (LEFM) 1.10^{-10} (Effective)	1.2 (LEFM) 2.8 (Effective)	1.6 (LEFM) (Effective)

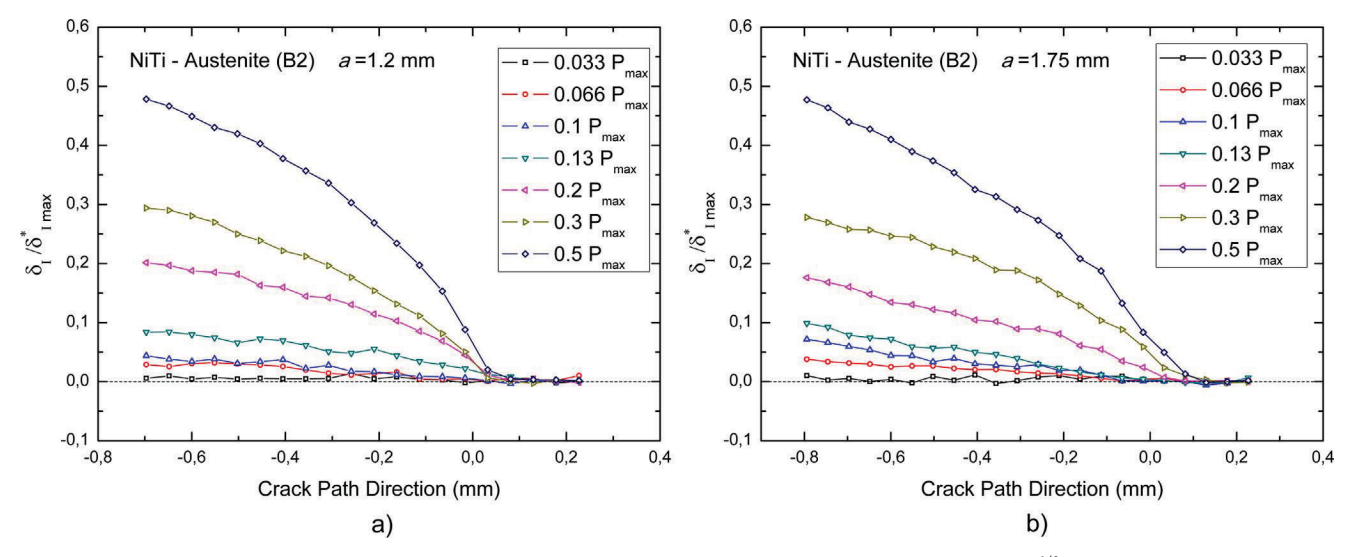


Fig. 10. Crack opening displacement for the austenitic structure: (a) crack length a=1.2 mm and stress intensity factor $\Delta K_{Ie}=3.1$ MPa·m^{1/2}; (b) crack length a=1.75mm and stress intensity factor $\Delta K_{Ie}=4.14$ MPa·m^{1/2}.

computed with the DIC method, by correlating images at $P_{\rm max}$ with respect to the reference one taken at $P_{\rm m}$.

Eq. (21) was adopted to fit the experimental crack opening displacement measured with the virtual extensometers, and the elastic modulus E was used as regression parameter. Fig. 13a shows a comparison between the analytical solution and the regressed data of the crack opening displacement.

The fitting procedure, performed on the measured crack opening displacement, provided very interesting information about the elastic modulus near the crack tip, as shown in Fig. 13b. In particular, the austenitic structure shows an almost constant trend of the Young's modulus with values close to 80 GPa. Only a small increasing trend is observed at the lowest values of the crack length, which can be attributed to measurement errors of the COD.

On the contrary, the martensitic structure exhibits a marked increasing trend of the Young's modulus as a function of the crack length. In fact, at the beginning of the test, when the crack length and the detwinned zone at the crack tip are small, the elastic modulus is expected to be very close to that observed by the tensile test, i.e. it is around 40 GPa. When the crack grows the elastic modulus increases, meaning that a redistribution of the martensitic variants, along the load

direction, is happening. The trend tends to stabilize with further increasing the crack length denoting that all the variants are completely reoriented. Finally, in the near fracture zone a Young's modulus close to 90 GPa is estimated. This result seems to be in agreement with observations reported in [43] where the elastic modulus of the oriented martensite was measured to be around 120 GPa, which is actually higher than that of austenite.

Obtained data, reported in Fig. 13b, were used as input parameters to calculate the new crack propagation curves. In particular, for each measurement point, the corresponding elastic modulus obtained from Eq. (21) was used to calculate the effective SIF from Eq. (14). From the new calculations, not big difference was obtained for the austenitic (B2) structure, in fact results are identical to the one reported in Fig. 8b. Instead, a completely new trend was recorded for the martensite (B19'), Fig. 14, and it well approaches the LEFM calculated behavior. This latter result can justify the reason why no big closure effect was measured with the virtual extensometer analysis.

4. Conclusions

Fatigue crack growth analysis on NiTi edge-notched samples, with

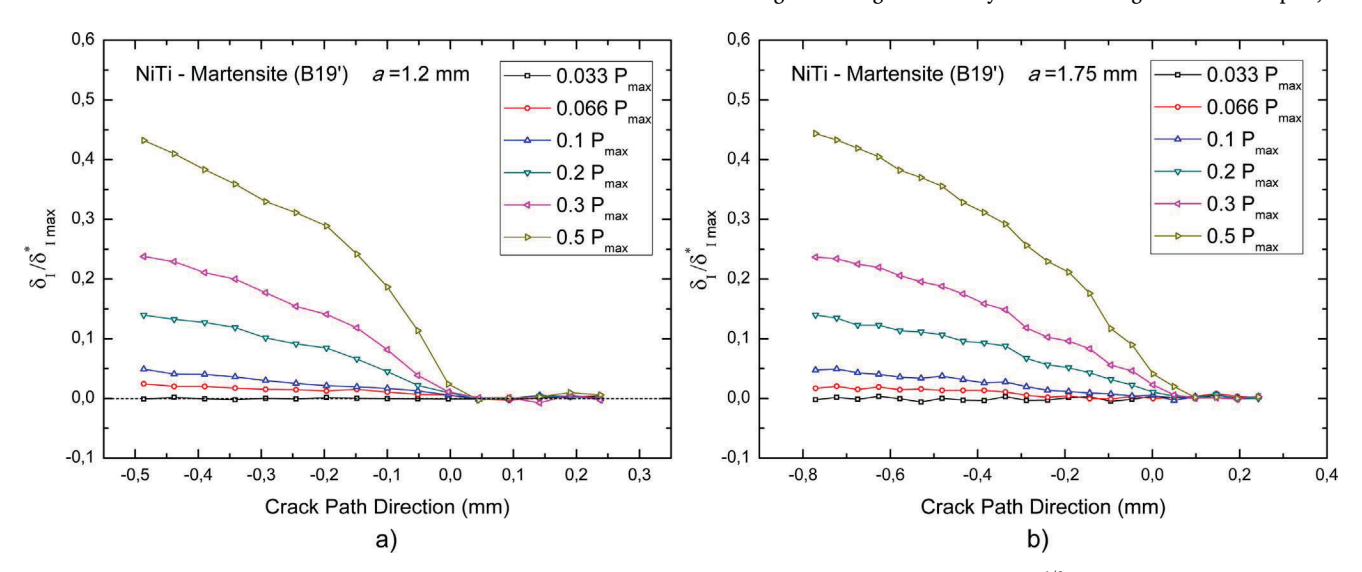


Fig. 11. Crack opening displacement for the martensitic structure: (a) crack length $a=1.2\,$ mm and stress intensity factor $\Delta K_{Ie}=5.32\,$ MPa·m^{1/2}; (b) crack length $a=1.75\,$ mm and stress intensity factor $\Delta K_{Ie}=8.38\,$ MPa·m^{1/2}.

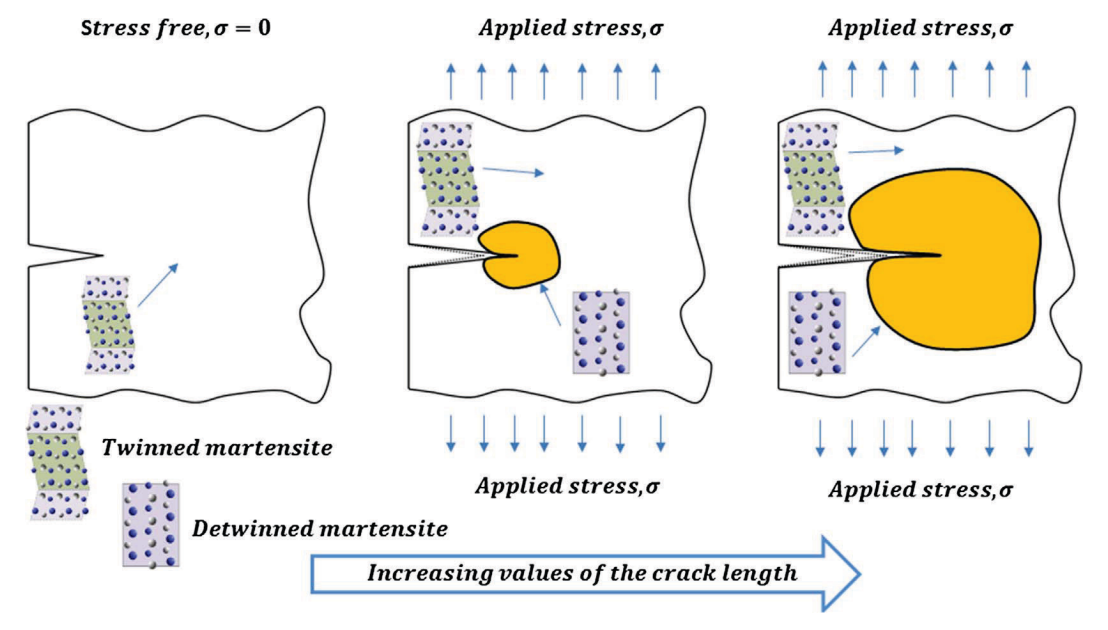


Fig. 12. Evolution of the oriented martensitic variants zone during the load history.

[0 1 2] crystallographic orientation, were carried out in this study with the aim to evaluate the crack growth rate of the stable austenite (B2) and stable martensite (B19') structures. Materials with the same composition were used and, consequently, tests were carried out at two different values of temperature, i.e. at $T=20\,^{\circ}\text{C}$ and $80\,^{\circ}\text{C}$. A proper numerical procedure was implemented to estimate the effective stress intensity factor and crack length, i.e. those taking into account the near crack tip non-linearity similarly to the Irwin's correction of the linear elastic fracture mechanics.

The procedure starts from the near crack tip displacements, measured with the Digital Image Correlation (DIC) technique, and by means of a least square regression approach, based on the William's series solution, is able to estimate the fracture parameters even when irreversibility occurs. The proposed approach needs the local elastic properties as input parameter. However, these latter are not easy to estimate, especially when dealing with the martensitic structure. In fact, as well known, the stress-induced transitions from multi-variant ("twinned") to single variant ("detwinned") arrangements cause a stiffness increase of the material.

To accurately estimate the effective elastic modulus, the crack

opening displacements measurement were calculated by DIC using virtual extensometers. The obtained results were fitted with the analytical solution of the crack opening displacement, based on the strip yield model, and the elastic modulus was extracted as regression parameter.

The obtained results from fatigue tests, show that austenitic structure has a lower fatigue threshold value, $\Delta K_{Ie,th} = 1.4 \text{ MPa} \cdot \text{m}^{1/2}$ compared to martensite $\Delta K_{Ie,th} = 3.3 \text{ MPa} \cdot \text{m}^{1/2}$, and a higher crack growth rate. Furthermore, it was demonstrated that, when dealing with martensite, the local elastic properties change, as a consequence of the variants reorientation, and this effect has to be taken into account for the fatigue crack growth characterization.

Finally, it is worth noting that data presented in this paper are very valuable because they are based on experiments performed on single crystal alloy and so they draw attention to the precise measurements near threshold. In fact, thanks to the absence of the grain boundary effects it has been possible to focus on the intrinsic matrix fatigue crack growth response.

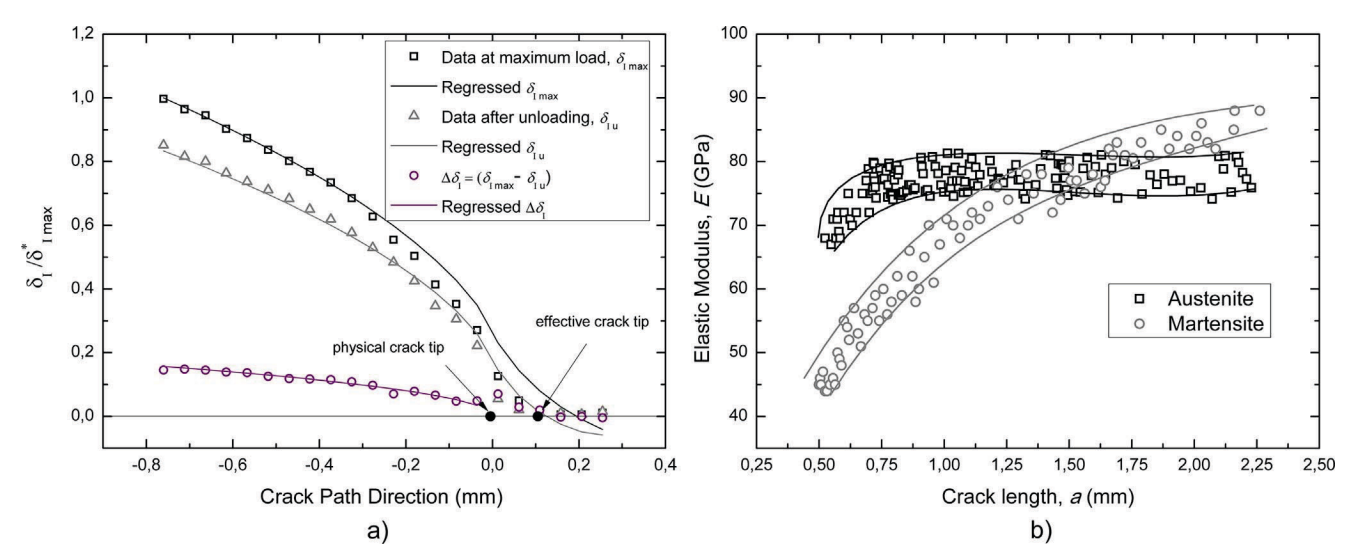


Fig. 13. (a) comparison between experimental and regressed crack opening displacements; (b) evolution of the local elastic modulus during the load history.

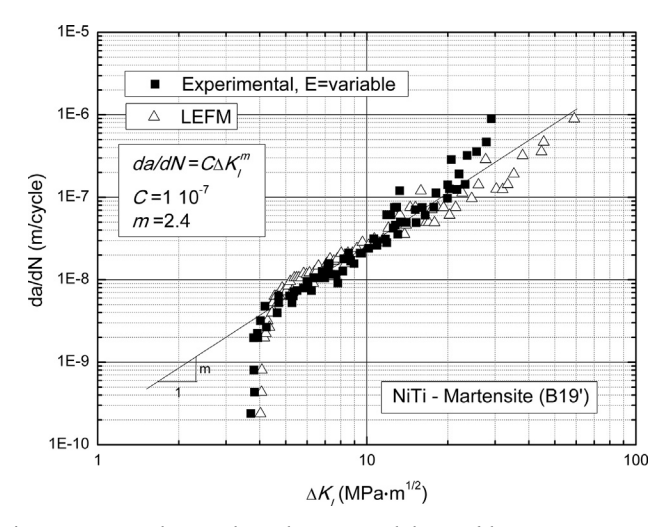


Fig. 14. comparison between the crack propagation behavior of the martensitic structure, obtained by using variable elastic properties at the crack tip, and the one calculated with the linear elastic fracture mechanics (LEFM).

Acknowledgement

Professor Huseyin Sehitoglu acknowledges partial support from NSF DMR-1709515, USA. We acknowledge Y. Wu (Graduate student, Illinois) assistance with orientation measurements of the sample.

References

- [1] Otsuka K, Wayman CM. Shape Memory Materials. Cambridge University Press;
- [2] Otsuka K, Ren X. Physical metallurgy of Ti–Ni-based shape memory alloys. Prog Mater Sci 2005;50:511–678.
- [3] Duerig TW, Melton KN, Stockel D, Wayman CM. Engineering Aspects of Shape Memory Alloys. Butterworth-Heinemann; 1990.
- [4] Melton N, Mercier O. Fatigue of NiTi thermoelastic martensites. Acta Metall 1979;27:137–44.
- [5] Melton N, Mercier O. The effect of the martensitic phase transformation on the low cycle fatigue behaviour of polycrystalline NiTi and CuZnAl alloys. Mater Sci Eng 1979;40(1):81–7.
- [6] Mckelvey AL, Ritchie RO. Fatigue-crack growth behavior in the superelastic and shape-memory alloy nitinol. Metall Mater Transactions A 2001;32:731–43.
- [7] Dauskardt RH, Duerig TW, Ritchie RO. Effects of in situ phase transformation on fatigue-crack propagation in titanium-nickel shape memory alloys. MRS Shape Memory Materials 1989;9:243–9.
- [8] Holtz RL, Sadananda K, Imam MA. Fatigue thresholds of Ni-Ti alloy near the shape memory transition temperature. Int J Fatigue 1999;21:137–45.
- [9] Stankiewicz J, Robertson SW, Ritchie RO. Fatigue-crack growth properties of thinwalled superelastic austenitic Nitinol tube for endovascular stent. J Biomed Mater 2007;81:685–91.
- [10] Robertson SW, Ritchie RO. In vitro fatigue-crack growth and fracture toughness behavior of thin-walled superelastic nitinol tube for endovascular stents: a basis for defining the effect of crack-like defects. Biomaterials 2007;28:700–9.
- [11] Robertson SW, Ritchie RO. A fracture mechanics based approach to fracture control in biomedical devices manufactured from superelastic nitinol tube. J Biomed Mater Res Part B 2008;84:26–33.
- [12] Baxevanis T, Lagoudas DC. Fracture mechanics of shape memory alloys: review and perspectives. Int J Fract 2015;191:191–213.
- [13] Robertson SW, Mehta A, Pelton AR, Ritchie RO. Evolution of crack-tip transformation zones in superelastic Nitinol subjected to in situ fatigue: a fracture mechanics and synchrotron X-ray microdiffraction analysis. Acta Mater 2007;55:6198–207.
- [14] Daymond MR, Young ML, Almer JD, Dunand DC. Strain and texture evolution during mechanical loading of a crack tip in martensitic shape-memory NiTi. Acta Mater 2007;55:3929–42.
- [15] Gollerthan S, Young ML, Baruj A, Frenzel J, Schmahl WW, Eggeler G. Fracture mechanics and microstructure in NiTi shape memory alloys. Acta Mater 2009;57:1015–25.
- [16] Gollerthan S, Young ML, Neuking K, Ramamurty U, Eggeler G. Direct physical evidence for the back-transformation of stress-induced martensite in the vicinity of cracks in pseudoelastic NiTi shape memory alloys. Acta Mater 2009;57:5892–7.
- cracks in pseudoelastic NiTi shape memory alloys. Acta Mater 2009;57:5892–7.
 [17] Maletta C, Bruno L, Corigliano P, Crupi V, Guglielmino E. Crack-tip thermal and mechanical hysteresis in shape memory alloys under fatigue loading. Mater Sci Eng A 2014;616:281–7.
- [18] Daly S, Miller A, Ravichandran G, Bhattacharya K. Experimental investigation of crack initiation in thin sheets of nitinol. Acta Mater 2007;55:6322–30.
- [19] Wu Y, Ojha A, Patriarca L, Sehitoglu H. Fatigue crack growth fundamentals in shape memory alloys. Shape Memory Superelasticity 2015;1:18–40.

- [20] Sgambitterra E, Maletta C, Furgiuele F. Investigation on crack tip transformation in NITI Alloys: effect of the temperature. Shape Memory Superelasticity 2015;1:275–83
- [21] Sgambitterra E, Lesci S, Maletta C. Effects of higher order terms in fracture mechanics of shape memory alloys by digital image correlation. Procedia Eng 2015;109:457–64.
- [22] Sgambitterra E, Bruno L, Maletta C. Stress induced martensite at the crack tip in NiTi alloys during fatigue loading. Frattura ed Integrità Strutturale 2014;30:167–73.
- [23] Maletta C, Sgambitterra E, Niccoli F. Temperature dependent fracture properties of shape memory alloys: novel findings and a comprehensive model. Sci Rep 2016;6:17.
- [24] Sgambitterra E, Maletta C, Furgiuele F. Temperature dependent local phase transformation in shape memory alloys by nanoindentation. Scripta Mater 2015;101:64–7.
- [25] Maletta C, Niccoli F, Sgambitterra E, Furgiuele F. Analysis of fatigue damage in shape memory alloys by nanoindentation. Mater Sci Eng A 2017;684:335–43.
- [26] Dy Li, Wu XF, Ko T. Texture of Ti-51.5 at% Ni rolling plate and its effect on the all-round shape memory effect. Acta Metall 1990;38:19–24.
- [27] Yuan W, Yi S. Pseudo-elastic strain estimation of textured TiNi shape memory alloys. Mater Sci Eng A 1999;271:439–48.
- [28] Frick CP, Ortega AM, Tyber J, Gall K, Maier HJ. Multiscale structure and properties of cast and deformation processed polycrystalline NiTi shape-memory alloys. Metall Mater Trans A 2004;35:2013–25.
- [29] Sato H, Takezawa K, Sato S. The 2nd martensitic-transformation stress-induced in Cu-Zn-Al alloy single-crystals. Mater Trans, JIM 1984;25:324–31.
- [30] Otsuka K, Sakamoto H, Shimizu K. Successive stress-induced martensitic transformations and associated transformation pseudoelasticity in CuAlNi alloys. Acta Metall 1979;27:585–601.
- [31] Matsumoto O, Miyazaki S, Otsuka K, Tamura H. Crystallography of martensitic transformation in Ti-Ni single crystals. Acta Metall 1987;35:2137–44.
- [32] Zuev L, Kartashova N, Danilov V, Chumlyakov Y, Poletika T. Strain localization in a material with transformation-induced plasticity (NiTi single crystals). Tech Phys 1996;41:1189–92.
- [33] Sehitoglu H, Jun J, Zhang X, Karaman I, Chumlyakov Y, Maier H, et al. Shape memory and pseudoelastic behavior of 51.5%Ni-Ti single crystals in solutionized and overaged state. Acta Mater 2001;49:3609–20.
- [34] Gall K, Yang N, Sehitoglu H, Chumlyakov Y. Fracture of precipitated NiTi shape memory alloys. Int J Fract 2001;109:189–207.
- [35] Creuziger A, Bartol LJ, Gall K, Crone WC. Fracture in single crystal NiTi. J Mech Phys Solids 2008;56:2896–905.
- [36] Gall K, Sehitoglu H, Chumlyakov YI, Zuev YL, Karaman I, crystal The role of coherent precipitates in martensitic transformations in single, et al. Scr Mater 1998;39:699–705.
- [37] Sehitoglu H, Karaman I, Anderson R, Zhang X, Gall K, Maier HJ, et al. Compressive response of NiTi single crystals. Acta Mater 2000;48:3311–26.
 [38] Miyazaki S, Otsuka K, Wayman CM. The shape memory mechanism associated with
- [38] Miyazaki S, Otsuka K, Wayman CM. The shape memory mechanism associated with the martensitic transformation in Ti-Ni alloys-I Self-accommodation. Acta Metall 1989;37:1873–84.
- [39] Alkan S, Sehitoglu H. Dislocation core effects on slip response of NiTi-a key to understanding shape memory. Int J Plasticity 2017;97:126–44.
- [40] Sih GC, Paris PC, Irwin GR. On crack in rectilinearly anisotropic bodies. Int J Fracture Mech 1965;1:189–203.
- [41] Liu Y, Xie Z, Van Humbeeck J, Delaey L. Some results on the detwinning process in NiTi shape memory alloys. Scr Mater 1999;41:1273–81.
- [42] Sehitoglu H, Hamilton R, Canadinc D, Zhang XY, Gall K, Karaman I, et al. Detwinning in NiTi alloys. Metall Mater Trans A 2003;34:5–13.
- (43) Sehitoglu H, Karaman I, Anderson R, Zhang X, Gall K, Maier HJ, et al. Compressive response of niti single crystals. Acta Mater 2000;48:3311–26.
- [44] Sehitoglu H. Crack opening and closure in fatigue. Eng Fract Mech 1985;21:329–39.
 [45] Gall K, Sehitoglu H, Chumlyakov YI, Kireeva IV, Maier HJ. The influence of aging
- [45] Gall K, Sehitoglu H, Chumlyakov YI, Kireeva IV, Maier HJ. The influence of aging on critical transformation stress levels and martensite start temperatures in NiTi: Part II-discussion of experimental results. J Eng Mater Technol 1999;121:28–37.
- [46] Wang J, Sehitoglu H. Martensite modulus dilemma in monoclinic NiTi-theory and experiments. Int J Plasticity 2014;61:17–31.
- [47] Zhan Y, You Y, Moumni Z, Anlas G, Zhu J, Zhan W. Experimental and theoretical investigation of the frequency effect on low cycle fatigue of shape memory alloys. Int J Plasticity 2017;90:1–30.
- [48] Maletta C, Furgiuele F. Fracture control parameters for NiTi based shape memory alloys. Int J Solids Struct 2011;20:597–604.
- [49] Maletta C, Furgiuele F. Analytical modeling of stress-induced martensitic transformation in the crack tip region of nickel-titanium alloys. Acta Mater 2010;58(1):92–101.
- [50] Maletta C, Young ML. Stress-induced martensite in front of crack tips in niti shape memory alloys: modeling versus experiments. J Mater Eng Perform 2011;20(4–5):597–604.
- [51] Maletta C, Sgambitterra E, Furgiuele F. Crack tip stress distribution and stress intensity factor in shape memory alloys. Fatigue Fract Eng M 2013;36(9):903–12.
- [52] Baxevanis T, Lagoudas DC. A mode I fracture analysis of a center-cracked infinite shape memory alloy plate under plane stress. Int J Fract 2012;175:151–66.
- [53] Ren G, Sehitoglu H. Interatomic potential for the NiTi alloy and its application. Comp Mater Sci 2016;123:19–25.
- [54] Tada H, Paris PC, Irwin GR. The stress analysis of cracks handbook. 2nd ed. MO: St. Louis; 1985.
 [55] Hertzberg RW. Deformation and fracture mechanics of engineering materials. New
- York: Wiley; 1989. [56] Vaidyanathan R, Dunand DC, Ramamurty U. Fatigue crack-growth in shape-
- memory NiTi and NiTi-TiC composites. Mat Sci Eng A 2000;289:208–16.
- [57] Alkan S, Sehitoglu H. Nonuniqueness of the fatigue threshold. Int J Fatigue 2017;104:309–21.